applied sciences

MDPI

Article

Experimental and Molecular Dynamics Simulation Study on Sulfate Corrosion Resistance of Cellulose-Nanocrystal-Modified ECC

Lei Yu [1], Xiaolong Xu [1], Songyuan Ni [1], Dan Meng [1], Xue Meng [2] and Binghua Xu [1,*]

[1] School of Architectural Engineering, Qingdao Agricultural University, Qingdao 266109, China; 201201001@qau.edu.cn (L.Y.); xuxiaolong@qau.edu.cn (X.X.); nisy@qau.edu.cn (S.N.); mengdan@qau.edu.cn (D.M.)
[2] College of Architecture and Environment, Sichuan University, Chengdu 610041, China; 20212204010@stu.qau.edu.cn
* Correspondence: 201201050@qau.edu.cn

Abstract: In this study, cellulose nanocrystals (CNs) were utilized to enhance the mechanical properties and sulfate corrosion resistance of engineered cementitious composites (ECCs). The results of compressive strength and uniaxial tensile tests demonstrated that the incorporation of CNs significantly improved the compressive strength, strain rate, tensile strength, and sulfate corrosion resistance of ECC specimens. Scanning electron microscopy (SEM) observations revealed that the addition of CNs facilitated the formation of increased amounts of ettringite and calcium silicate hydrate (C-S-H) in the matrix, enhancing the hydration degree of the cementitious system and increasing the overall density of the ECC structure. Molecular dynamics simulations were employed to investigate the interactions between CN, C-S-H, water molecules, and sulfate ions (SO_4^{2-}) while also calculating the kinetic parameters of atoms at the interface. These simulations provided insights into the microstructural strengthening mechanism of CNs in improving the sulfate corrosion resistance of ECCs. The results indicated that CNs adsorb onto C-S-H via Ca-O and H-O coordination, forming a protective layer that inhibits the penetration of SO_4^{2-} and water molecules into the C-S-H structure. Additionally, CNs form hydrogen bonds with SO_4^{2-} and water molecules, which restricts their diffusion and reduces their coordination with the C-S-H interface and the dissolution of SO_4^{2-} and water to the hydration product, thereby enhancing the sulfate corrosion resistance of ECCs.

Keywords: engineered cementitious composite; cellulose nanocrystals; molecular dynamics; interfacial adsorption

check for updates

Academic Editor: Luigi Biolzi

Received: 16 February 2025
Revised: 5 March 2025
Accepted: 13 March 2025
Published: 14 March 2025

Citation: Yu, L.; Xu, X.; Ni, S.; Meng, D.; Meng, X.; Xu, B. Experimental and Molecular Dynamics Simulation Study on Sulfate Corrosion Resistance of Cellulose-Nanocrystal-Modified ECC. *Appl. Sci.* **2025**, *15*, 3205. https://doi.org/10.3390/app15063205

Copyright: © 2025 by the authors. Licensee MDPI, Basel, Switzerland. This article is an open access article distributed under the terms and conditions of the Creative Commons Attribution (CC BY) license (https://creativecommons.org/licenses/by/4.0/).

1. Introduction

Concrete is the most commonly used building material in engineering construction. However, the interface transition area between the cement slurry and aggregate is weak, which can easily become the trigger point for micro-cracks. This characteristic makes concrete materials highly brittle and prone to damage when subjected to loads or impacts. Li et al. [1] optimized the interfacial performance of fiber and matrix and invented engineered cementitious composites (ECCs) with a strain rate of up to 2%. Due to its superior engineering performance, the ECC has been applied in many projects [2–8].

At present, many scholars have conducted research on the ratio design of ECCs and proposed using a variety of auxiliary cementitious materials such as fly ash, silica fume, slag, rice husk ash, wood ash, and recycled micropowder to prepare ECCs. These studies have found that the use of auxiliary gelling materials can increase the degree of hydration of

the matrix, enhance the density of the ECC structure, and enhance the various parameters of ECCs while reducing the amount of cement [9–13].

It is found that the corrosion of sulfate on a concrete structure is the most critical factor affecting its service life [14]. With the development of industry, the emission of sulfur dioxide increases, making the sulfate exist in rainwater, groundwater, and soil, which makes concrete materials vulnerable to sulfate corrosion. Sulfates will react with hydrated products, promoting the formation of expansive products, resulting in the water absorption, cracking, and damage of local structures inside the concrete substrate, thereby accelerating and reducing the transmission of chloride ions and other harmful substances inside the concrete and ultimately significantly reducing the durability of concrete [15–17]. In addition, the amount of gelling material in the ECC material system is very high, which makes the matrix contain a lot of calcium, making the structure of the ECC more easily corroded by sulfate. The cost of an ECC is 5–10 times that of ordinary concrete. Under the premise of superior performance, its durability should also be guaranteed to extend its useful life. It can be seen that it is necessary to explore the sulfate corrosion resistance of ECCs and propose efficient and environmentally friendly enhancement solutions.

In recent years, research on nanomaterials in civil engineering materials has attracted much attention. Research by Abdulkadir et al. [18] found that graphene oxide (GO) can significantly improve the mechanical properties, reduce the drying shrinkage and sulfate erosion of ECCs [19], and significantly improve the impact resistance, elastic modulus, and Poisson ratio of ECCs. Liu et al. [20] used carbon nanotubes to enhance the durability of concrete and conducted freeze–thaw cycle tests on the samples under different salt corrosion. The results show that after 1500 salt freezing cycles, the concrete mass loss is not large, and the microstructure remains relatively dense. Research by Mohseni et al. [21] found that nanomaterials such as SiO_2, Al_2O_3, and TiO_2 play an important role in improving the performance of cement-based materials. In summary, it can be seen that the research direction of nano-enhanced ECC performance is feasible. However, the preparation process of these carbon nanomaterials is complicated, and the preparation time is long, which leads to high production costs. Concrete is a high-consumption building material, and the high cost of carbon nanomaterials limits their application in engineering.

Cellulose nanocrystals (CNs) are environmentally sustainable nanomaterials derived from agricultural solid waste [22]. Their preparation only needs two steps of crushing and hydrolysis, and the preparation cost is much lower than graphene oxide [23]. When CNs are incorporated as a reinforcement in mortar and concrete, they can significantly enhance the mechanical properties and durability of the composite [24–26]. However, limited research has been conducted on the use of CNs as an enhancement component in ECCs to improve their durability. Furthermore, due to the nanoscale dimensions of the CN and matrix, the mechanisms governing the interactions between nanomaterials and hydrated products at the adsorption interface are challenging to characterize. To address the interfacial interaction, some researchers have employed molecular dynamics simulations to investigate atomic bonding, diffusion, and micromechanical properties at the interface, examining the adsorption and diffusion behaviors and establishing a link between interface characteristics and the macroscopic mechanical properties of the composite material system [27–33].

This study investigates the use of CNs as a reinforcement material in ECCs and explores its impact on compressive strength, strain rate, and sulfate corrosion resistance. Molecular dynamics simulations were employed to analyze the interactions between C-S-H, CN, and a sodium sulfate solution, thereby elucidating the mechanism by which CNs enhance the sulfate corrosion resistance of ECCs.

2. Materials and Methods

The composition of the ECC is shown in Table 1. The mass ratio of cement, silica fume, and fly ash in the binder system is 7:2:1, the mass ratio of standard sand to cementitious materials is 0.3, the water-to-binder ratio is 0.22, the polycarboxylate superplasticizer is added at 0.02 by mass of cementitious materials, and the polyethylene (PE) fiber content is 2% by volume of the sample. CN-ECC samples were prepared by incorporating CNs into the mix at mass ratios of 0.05%, 0.10%, 0.15%, and 0.20% of the cementitious materials.

Table 1. The proportion of ECCs.

Binder (100%)			PE (vol)	Water	PCE	Sand
Cement	Silica Fume	Fly Ash				
70	20	10	2%	22	2	30

The sample preparation procedure is as follows: first, the dry materials, including cement, silica fume, fly ash, and sand, were mixed in a mortar mixer at low speed for 3 min. Water, a water-reducing agent, and CNs were then added to the dry mix and stirred at high speed for 1 min. Subsequently, PE fibers were introduced into the slurry, followed by further mixing for 3 min.

The binder material was sourced from Jiuqi Building Materials Co., Ltd., (Yantai, China) with the cement being ordinary Portland cement (P·O 42.5). The CN was obtained from Zhejiang Yuewei New Material Technology Co., Ltd., (Hangzhou, China) and is a white liquid (Figure 1a) with a TEM and AFM morphology shown in Figure 1b,c. The CN has a diameter ranging from 15 to 20 nm and a length between 200 and 500 nm. The PE fiber, sourced from Guangdong Teveron New Materials Application Co., Ltd., (Shenzhen, China) has a length of 9 mm and a diameter of 12 μm.

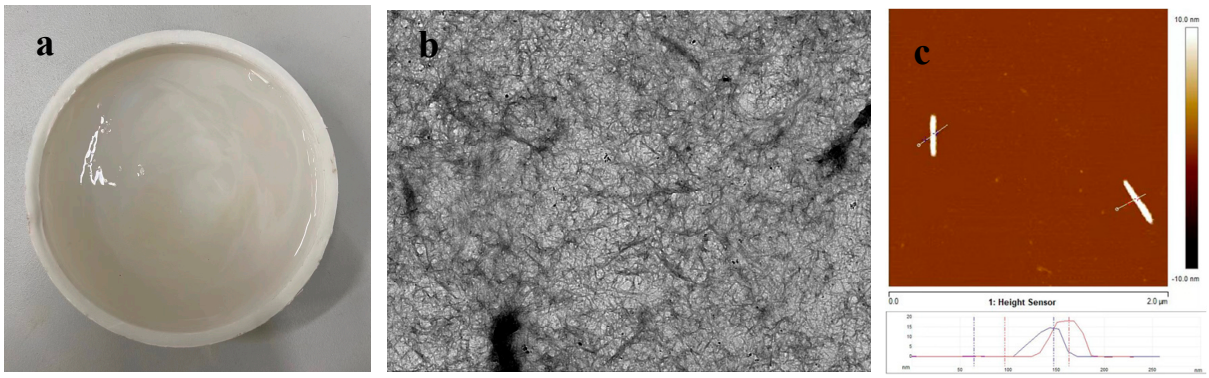


Figure 1. The morphology of a CN. (**a**) CN gel, (**b**) TEM, (**c**) AFM.

A uniaxial tensile test was carried out by a MTS-universal mechanical (Eden Prairie, MN, USA) testing machine to analyze the ECC's strain rate and tensile strength. The sample and instrument for the uniaxial tensile test are shown in Figure 2. The testing machine is adopted by displacement control, and the loading speed is 0.5 mm/min [31]. As for the compressive strength test, the sample with the size of 100 mm × 100 mm × 100 mm was prepared. This study refers to the GB/T50082-2009 standard [34] for experimentation with the sulfate corrosion resistance of the ECC. The sample should be soaked in a 5% Na_2SO_4 solution until it reaches corrosion age. Then, one should take the sample out, dry the surface of the sample, and test its strength and strain rate.

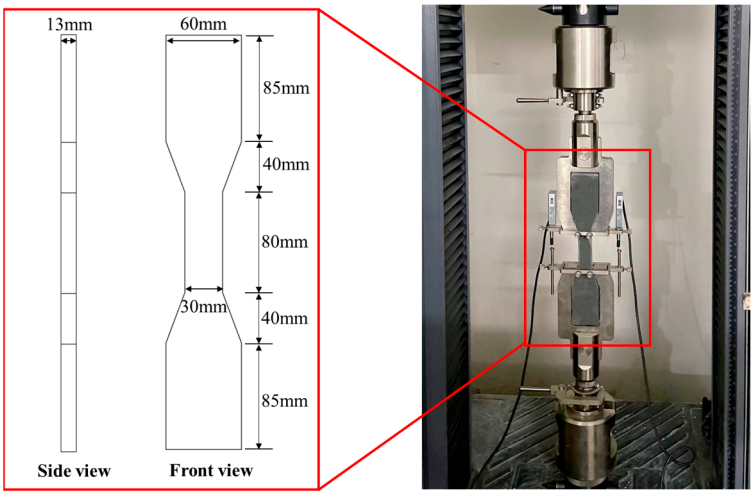


Figure 2. The sample and instrument for the uniaxial tensile test.

3. Test Results and Discussions

3.1. Effect of CN on Compressive Strength and Tensile Properties of ECC

Nanomaterials have been shown to significantly enhance the properties of composite materials. However, they are susceptible to agglomeration, necessitating an investigation into the optimal inclusion level of CNs to enhance the performance of ECCs. The compressive strength data for the ECC samples at 28 d are presented in Figure 3. As observed, the compressive strength of the control sample (without CNs) was 75.2 MPa. The compressive strengths of the CN-ECC samples with 0.05%, 0.10%, 0.15%, and 0.20% CN were 77.3, 81.9, 84.2, and 82.1 MPa, respectively. These values represent increases of 2.79%, 8.91%, 12.0%, and 9.18% compared to the control group. This enhancement is likely due to the nanoscale CN filling the internal pores of the cement matrix and improving the interfacial bonding between the PE and the matrix [35], which enables the sample to withstand higher loads. However, when the CN content reached 0.20%, the compressive strength slightly decreased compared to the 0.15% CN sample. At higher CN dosages, the reinforcing effect on the ECC compressive strength appears to diminish. This could be attributed to the formation of hydrogen bonds between the hydrophilic groups on the surface of the CN, leading to the agglomeration of the CN chains, which prevents effective dispersion within the cement matrix and limits its reinforcing potential [36].

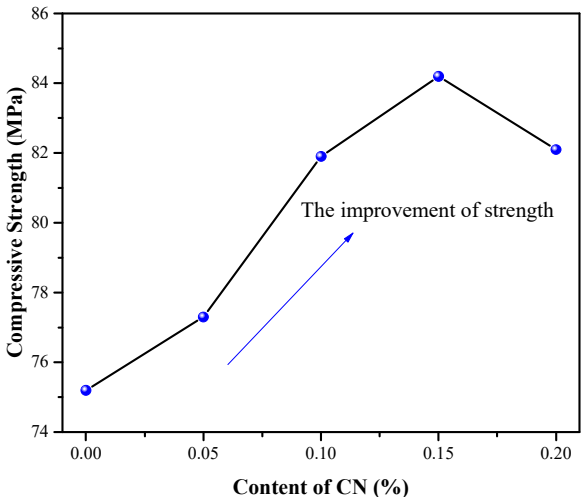


Figure 3. The compressive strength results of the ECC.

The uniaxial tensile test results for the ECC samples aged for 28 d are presented in Figure 4. Three specimens were tested per sample group, and the average value was taken as the representative result. The strain rate of the control group (without a CN) was 3.62%. For CN-ECC samples incorporating 0.05%, 0.10%, 0.15%, and 0.20% CN, the strain rates were 4.01%, 4.53%, 5.61%, and 5.42%, respectively. The incorporation of CNs enhances the strain rate of ECC samples, with the effect progressively increasing as the CN content rises, though a slight decrease in strain rate is observed at 0.20% CN content. A hydrophilic CN not only fills the internal pores but also interacts with PE fibers and C-S-H, thereby improving the interfacial bond between the PE fibers and the matrix [35]. This interaction, facilitated by the CN, enhances the bridging effect of the PE fibers within the matrix, distributing the applied load more uniformly and mitigating brittle cracking in cement-based materials, ultimately leading to an improvement in the strain rate of ECCs. The tensile strengths of the five ECC variants are 6.21 MPa, 6.52 MPa, 6.82 MPa, 6.82 MPa, and 6.81 MPa, respectively. The addition of CNs effectively fills the internal pores within the cement matrix, enhances the compactness of the ECC structure, and consequently improves its tensile strength.

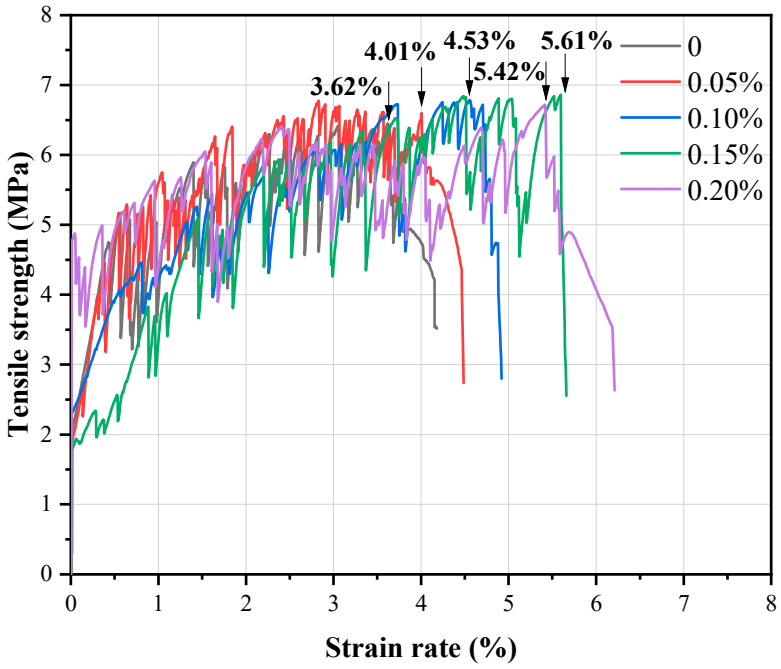


Figure 4. The uniaxial tension results of the ECC.

In conclusion, a CN content of 0.05% does not significantly enhance ECC performance, while the improvement observed with 0.20% CN is less pronounced than that achieved with the 0.15% sample group. Taking into account compressive strength, tensile properties, and economic considerations, it is reasonable to incorporate CNs at concentrations of 0.10% and 0.15% into the ECC.

3.2. Effect of CN on Sulfate Corrosion Resistance of ECC

When the hydration products are corroded by sulfate, SO_4^{2-} will react with the hydration products to produce expandable ettringite and gypsum. These products will not only generate expansion stress and expand local pores but also dissolve C-S-H and $Ca(OH)_2$ in the ECC matrix, destroy the ECC structure, and reduce its mechanical strength and durability [36].

The compressive strength results of an ECC subjected to sulfate corrosion at 30, 60, and 120 d are presented in Figure 5. As shown in the figure, the compressive strength of the ECC progressively decreases with increasing corrosion duration. For the sample group without a CN, the compressive strength after 30, 60, and 120 d of sulfate exposure decreased by 0.53%, 2.66%, and 6.78%, respectively. The compressive strength of the 0.1% CN sample group decreased by 0.49%, 1.59%, and 6.11%, while that of the 0.15% CN sample group decreased by 0.47%, 1.31%, and 5.42%, respectively. The structure of the ECC remains dense, and during the initial stages of sulfate exposure (30 and 60 d), the penetration of SO_4^{2-} and water molecules into the matrix is limited. Consequently, the compressive strength loss in all sample groups is minimal at these time points. However, at 120 d, a significant reduction in compressive strength is observed. Notably, the CN-containing samples exhibit a smaller strength loss compared to the control group. This improvement is attributed to the role of the CN in effectively filling the pores, enhancing the matrix density [37,38], restricting the diffusion of water and SO_4^{2-}, and mitigating the degradation of hydrated products by sulfate and water, thereby extending the service life of the ECC in aggressive environments.

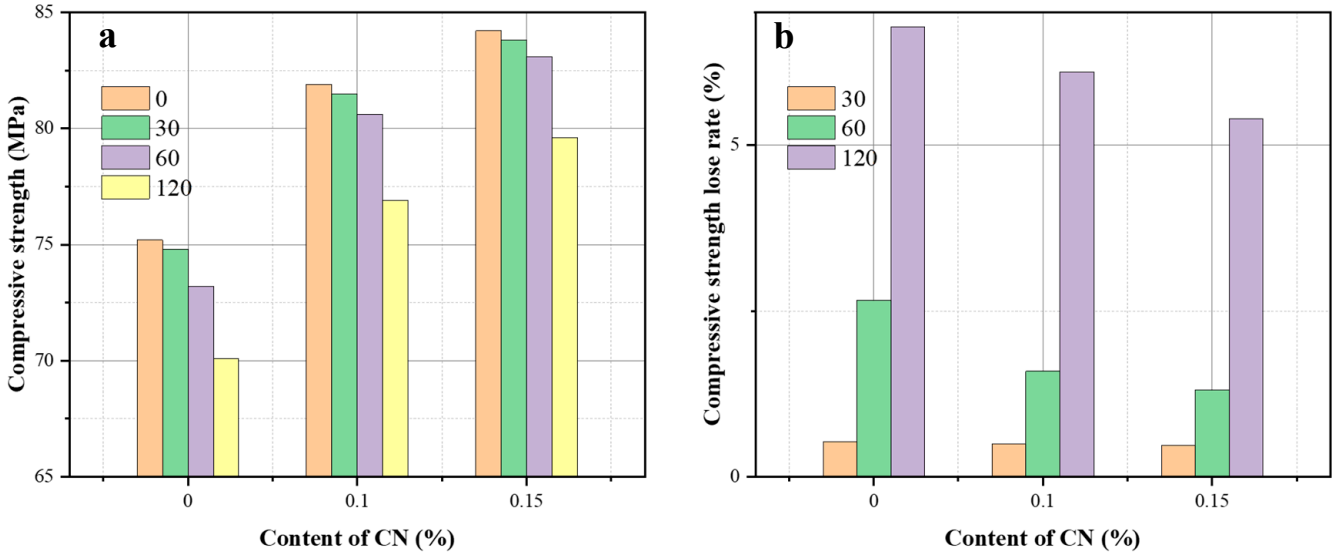


Figure 5. Compressive strength results of ECC after sulfate corrosion. (**a**) Compressive strength; (**b**) loss rate.

The uniaxial tensile test results of the ECC samples following sulfate corrosion are presented in Figure 6 (The arrow marks the ultimate strain rate on the stress-strain curve). For the control sample (Figure 6a), after 60 and 120 d of sulfate corrosion, the strain rate decreased to 3.51% and 3.32%, respectively, from the initial 3.62%, resulting in a strain loss of 3.04% and 8.29%. For the 0.10% CN-ECC sample group (Figure 6b), the strain rate reduced to 4.44% and 4.22% from the original 4.53%, with strain losses of 1.99% and 6.84%, respectively. For the 0.15% CN-ECC sample group (Figure 6c), the strain rate decreased to 5.51% and 5.26% from the initial 5.61%, showing strain losses of 1.78% and 6.23%.

It is obvious that the strain rate loss of the CN-ECC sample under sulfate corrosion is lower than that of the control group, and the CN can effectively alleviate the damage of sulfate on the ECC's tensile properties. Combined with the compressive strength, strain rate, and sulfate corrosion resistance, it can be seen that when the content of the CN is 0.15%, it has the strongest effect on improving the ECC's performance.

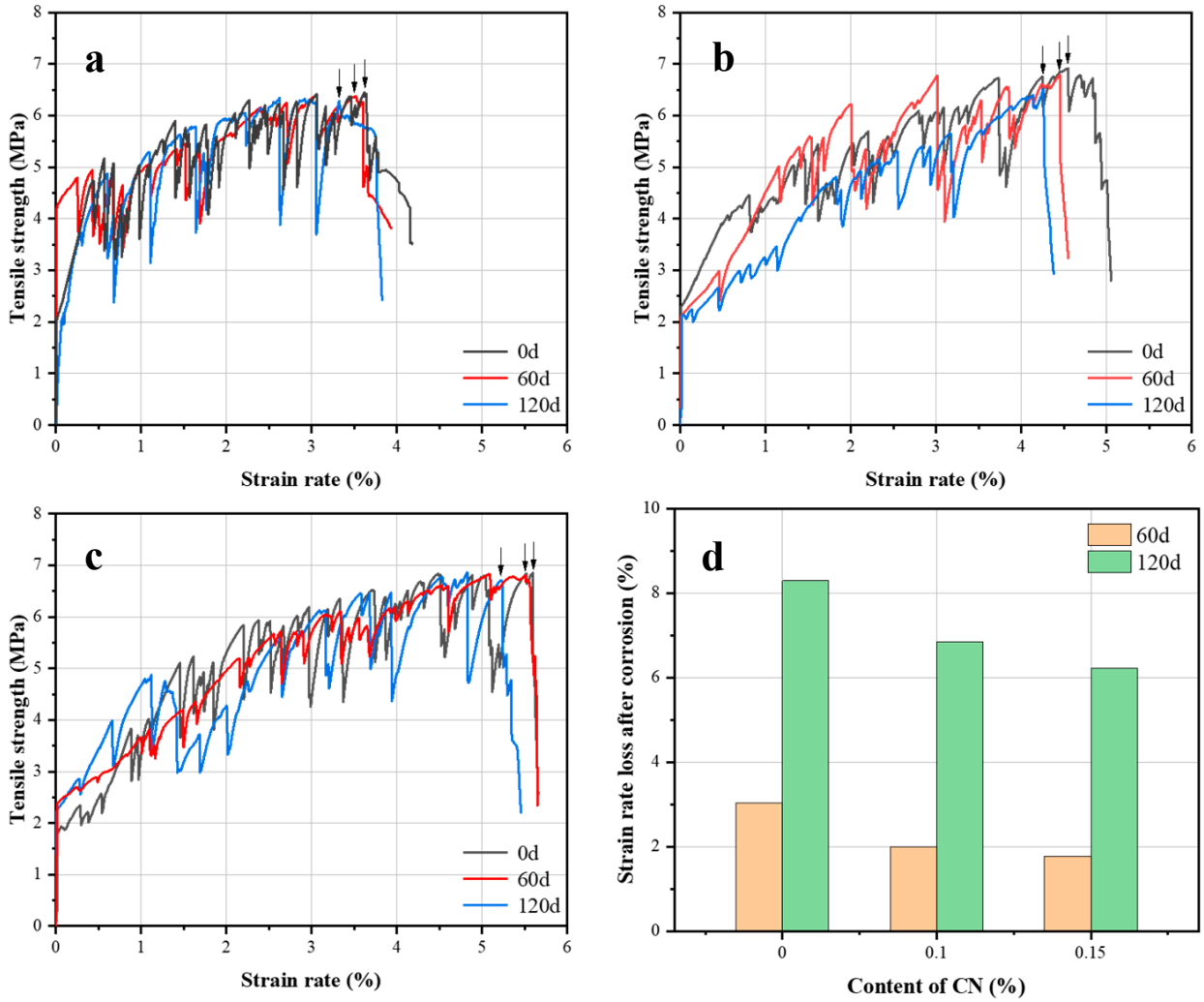


Figure 6. Tension results of ECC after sulfate corrosion. (**a**–**c**) Strain rate; (**d**) loss rate.

3.3. Micro-Morphology Inside the ECC Matrix

The compressive strength and strain rate of the ECC are closely associated with the internal structure of the matrix. Nanomaterials commonly influence the hydration process of cement, thereby affecting the density of the hydration matrix. Previous studies, utilizing various testing methods, have shown that CNs can enhance cement hydration and increase the density of the cement matrix [39–41]. Previous SEM-EDS results from our team showed that when a CN is added to the mortar, it will reduce the calcium–silicon ratio of the hydrated product and increase the density of the hydrated product [36,38]. In this study, scanning electron microscopy (SEM, Tescan-SEM4000Pro, Xian, China) was employed to observe the microstructure of the ECC matrix. Figure 7a–c display the microscopic morphology of the control sample group (without a CN), where a noticeable unhydrated region is present in the matrix. A substantial amount of spherical silica fume (SF) and a minor quantity of ettringite are observed within the matrix. In contrast, the hydrated morphology of the 0.15% CN-ECC sample, depicted in Figure 7d–f, exhibits significant differences. Here, the matrix structure becomes denser, with more silica fume consumed by the hydration reaction and the formation of increased amounts of ettringite (AFT) and C-S-H. The SEM results indicate that the incorporation of a CN alters the structure of the hydrated matrix, promoting the formation of additional hydration products, which in turn enhances the overall properties of the ECC.

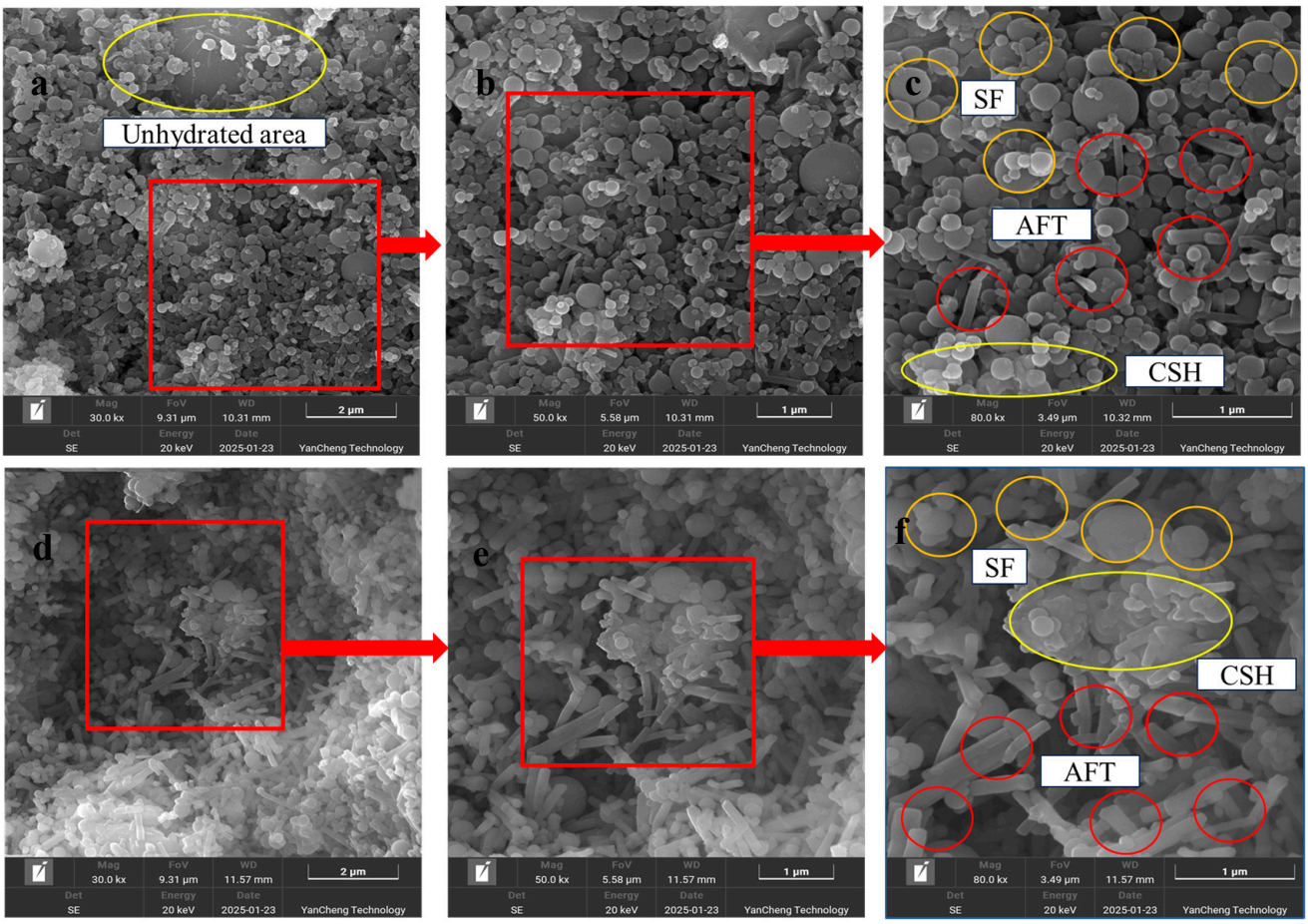


Figure 7. The hydration morphology of the ECC matrix. (**a**–**c**) Control sample; (**d**–**f**) 0.15% CN sample.

4. Molecular Dynamics Simulation

The CN and C-S-H are both nanoscale materials, and their interactions are challenging to characterize experimentally. To thoroughly investigate the strengthening mechanism of the CN on the sulfate corrosion resistance of the ECC, a more refined analytical scale is required. Given that nanoscale molecular dynamics simulations have been extensively applied to study the properties at the interface of composite materials, this study utilizes molecular dynamics simulations to explore the role of the CN in enhancing the sulfate corrosion resistance of the ECC.

4.1. Modeling Details

The modeling process of C-S-H is as follows: an 8 × 3 × 1 supercell was performed on the protocell of 11 Å Tobermolite [42], some SiO_2 was randomly deleted to make the model's calcium to silicon ratio 1.67, and then, the model was subjected to Monte Carlo water absorption [43]. Finally, a C-S-H calculation model with a density of 2.45 g/cm^3 and a lattice size of a = 44.64 Å, b = 22.17 Å, and c = 22.77 Å was obtained. CN chains are constructed in references [44,45]. Water molecules are SPC models. The C-S-H, CN, sodium sulfate solution, and composite adsorption models can be seen in Figure 8.

The CLAYFF force field effectively captures the atomic interactions within C-S-H [42], while the CVFF force field is well suited for modeling CN and Na_2SO_4 systems [46]. The simulations were carried out using LAMMPS, with the Nosé–Hoover method employed to maintain a constant temperature of 300 K. The simulation consisted of two stages: model relaxation and molecular dynamics simulation. Initially, the C-S-H and Na_2SO_4 aqueous solution models were relaxed for 500 ps under the NVE, NVT, and NPT ensembles to achieve

a more physically realistic density. Subsequently, the C-S-H and solution models were combined and subjected to simulations for 3000 ps under the NVT ensemble. Trajectories were recorded every 1000 steps, and the final 1000 ps of the trajectory was analyzed to examine the kinetic parameters during the adsorption process.

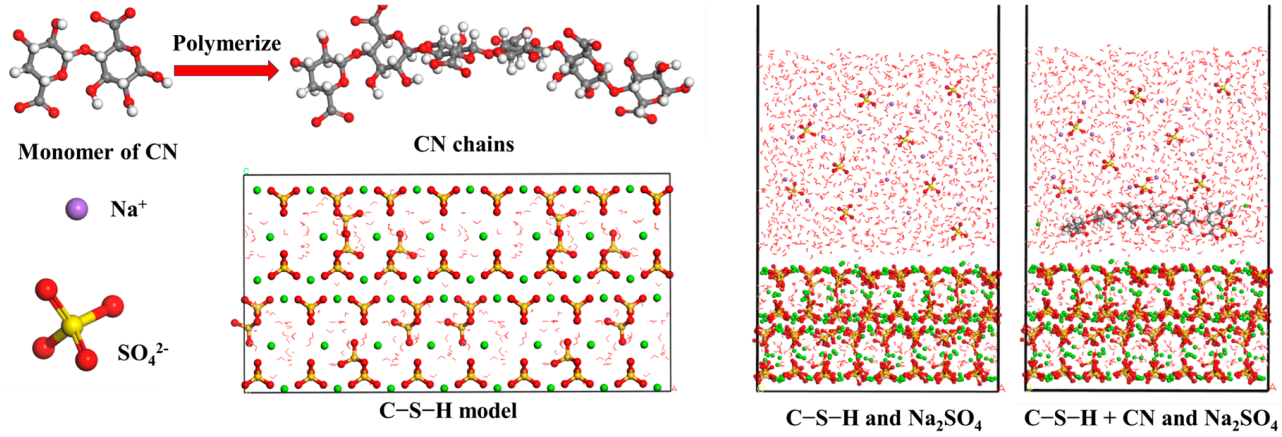


Figure 8. The C-S-H, CN, sodium sulfate solution, and composite adsorption models.

4.2. Adsorption Properties of CN and C-S-H Interfaces

The prevailing perspective on the enhancement mechanism of nanomaterials in cement-based composites suggests that nanomaterials interact with the matrix by adsorbing at the interface, influencing the behavior of water molecules, ion transport, and other properties, thereby affecting the overall characteristics of cement-based materials [47,48]. Therefore, it is essential to analyze the adsorption properties at the CN and C-S-H interfaces. Adsorption energy serves as a key parameter for intuitively assessing the adsorption behavior at these interfaces. In this study, the adsorption energy between the CN chain and the C-S-H interface was calculated for CN molecular chains in quantities of 1, 2, 3, and 4, respectively. The results, presented in Figure 9, reveal that the adsorption energy at the CN/C-S-H interface ranges from 900 to 1100 kcal/mol, indicating strong adsorption between the CN and C-S-H.

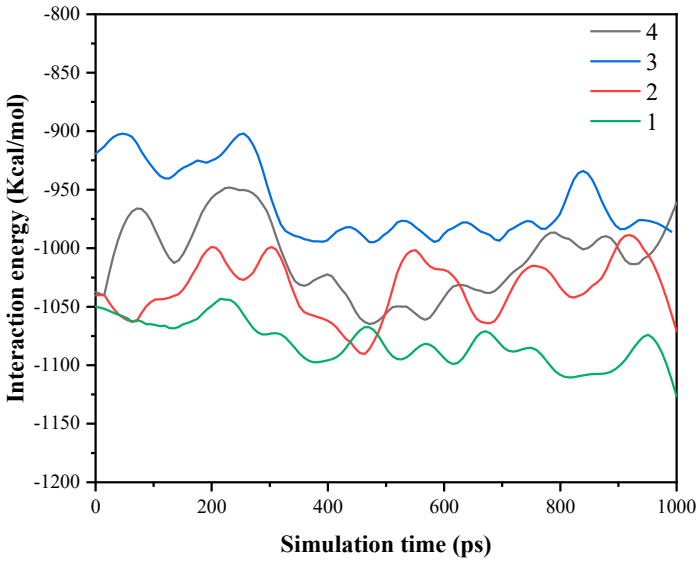


Figure 9. Interfacial energy results of CN/C-S-H.

When only one CN chain is present, the adsorption between the CN and C-S-H is optimal. As the number of CN chains increases to four, the adsorption energy between each

CN chain and C-S-H decreases from 1060 kcal/mol to 960 kcal/mol. This decrease suggests that an excessive number of CN chains weakens the interface adsorption properties. This effect may be attributed to the high density of hydrophilic groups on the CN surface, which, at higher concentrations, form hydrogen bonds that lead to chain entanglement. As a result, the contact area between the CN and C-S-H decreases, thus reducing the interface adsorption energy. In contrast, when only one CN chain is present, it can maintain a relatively straight conformation, allowing for more effective adsorption on the C-S-H interface. It is known from the experimental results that with the increased addition of the CN, its enhancement effect on ECC performance cannot be continuously increased. The interfacial adsorption energy results also indicate that the larger number of CN chains has a weaker interaction with C-S-H. Obviously, the interfacial adsorption energy results further verified the macroexperimental results.

The interface adsorption performance is closely associated with the contact area of the composite interface [49]. Atomic interactions induce shape alterations of the CN chain, thereby influencing the contact area between the CN and C-S-H. The radius of gyration (Rg) serves as a descriptor for the conformation of the model, where a larger Rg indicates a greater molecular surface area [50]. The Rg of the CN throughout the simulation is depicted in Figure 10. The evolution of Rg over time can be divided into three distinct stages: 10.84 in stage 1, 10.79 in stage 2, and stabilizing at 10.77 in stage 3. As the simulation progresses, Rg gradually decreases. During the transition from stage 1 to stages 2 and 3, the CN chain undergoes slight twisting and becomes more curved, though it largely maintains a relatively straight form.

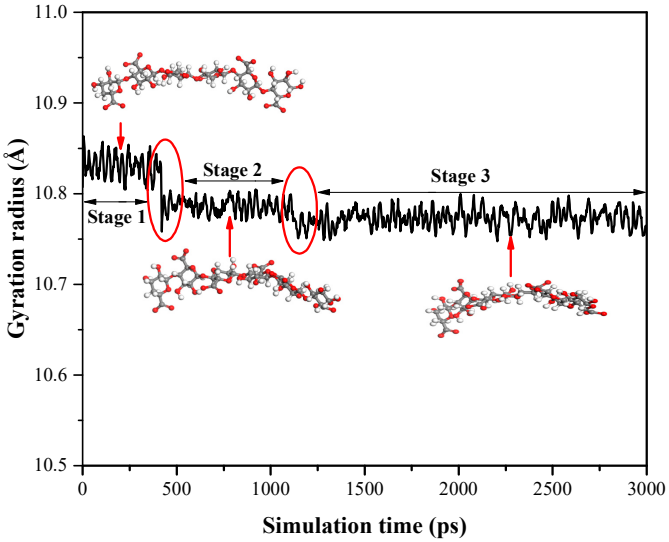


Figure 10. The gyration radius results of the CN.

The coordination between atoms can be analyzed through the radial distribution function (RDF). The first peak on the X-axis of the RDF curve for an atomic pair reflects the spatial correlation between the atoms [51]. The RDF results for the CN and C-S-H, water, and SO_4^{2-} are presented in Figure 11. A distinct peak appears at 1.6 Å between the O of the CN chain (O_{CN}) and Ca of C-S-H (Ca_C). Additionally, notable peaks are observed between O_{CN} and H in C-S-H (H_C), as well as between H in the CN chain (H_C) and O in C-S-H (O_C). This indicates that the CN chain can adsorb to C-S-H through Ca-O and H-O coordination. The RDF curves for H_{CN} and S and O atoms in SO_4^{2-} (S_S, O_S) also exhibit peaks, suggesting that the CN can adsorb SO_4^{2-} through hydrogen bonding.

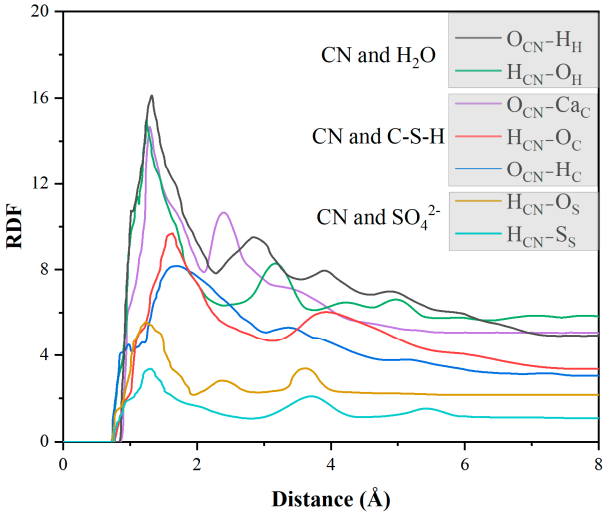


Figure 11. RDF results for CN/C-S-H, CN/SO_4^{2-}, and CN/water.

Figure 11 also demonstrates that O_{CN} and H_H (H in water), as well as H_{CN} and O_H (O in water), exhibit a peak at 1.5 Å, suggesting that the CN can also form hydrogen bonds with water molecules. This is attributable to the presence of numerous hydrophilic -OH and -COO^- groups on the CN, which enables its ability to adsorb water molecules. Additionally, the adsorption of the CN to water molecules influences the polarity of the water, which can be quantified through dipole moments. As depicted in Figure 12, the dipole moments of the CN solution and the free aqueous solution are 2.46 D and 2.44 D, respectively. The increased dipole moment of water in the presence of the CN further substantiates the hydrophilicity of the CN [51].

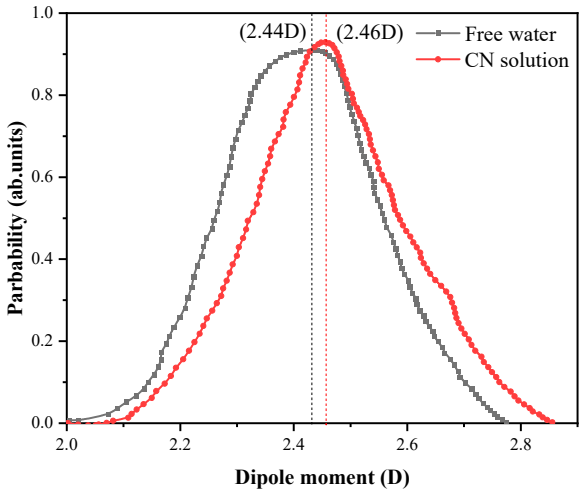


Figure 12. The dipole moment of solution.

4.3. Kinetics at the Adsorption Interface

The corrosion of the ECC by the sulfate solution can be understood in two aspects. First, there is the corrosion caused by water molecules, and second, there is the corrosion induced by SO_4^{2-}. RDF analysis indicates that the CN can be adsorbed between C-S-H, water, and SO_4^{2-}. These adsorptions will cause changes in the properties at the interface. It can be seen that the CN's enhancement mechanism of sulfate corrosion resistance can be understood by analyzing the kinetic characteristics of water molecules and SO_4^{2-} at the interface.

Figure 13a illustrates the RDF results between the Na_2SO_4 solution (without the CN) and C-S-H. A pronounced peak between Na^+ and O_C indicates a strong interaction between Na^+ and O_C, suggesting significant adsorption of Na^+ on the C-S-H surface. Additionally, a robust interaction between O_S and Ca_C is observed, implying that SO_4^{2-} reacts with C-S-H to form expansive products. Furthermore, coordination interactions between O_H-H_C, O_H-Ca_C, and H_O-O_C suggest that water molecules also interact with C-S-H, leading to the dissolution of hydration products and the degradation of C-S-H's internal structure.

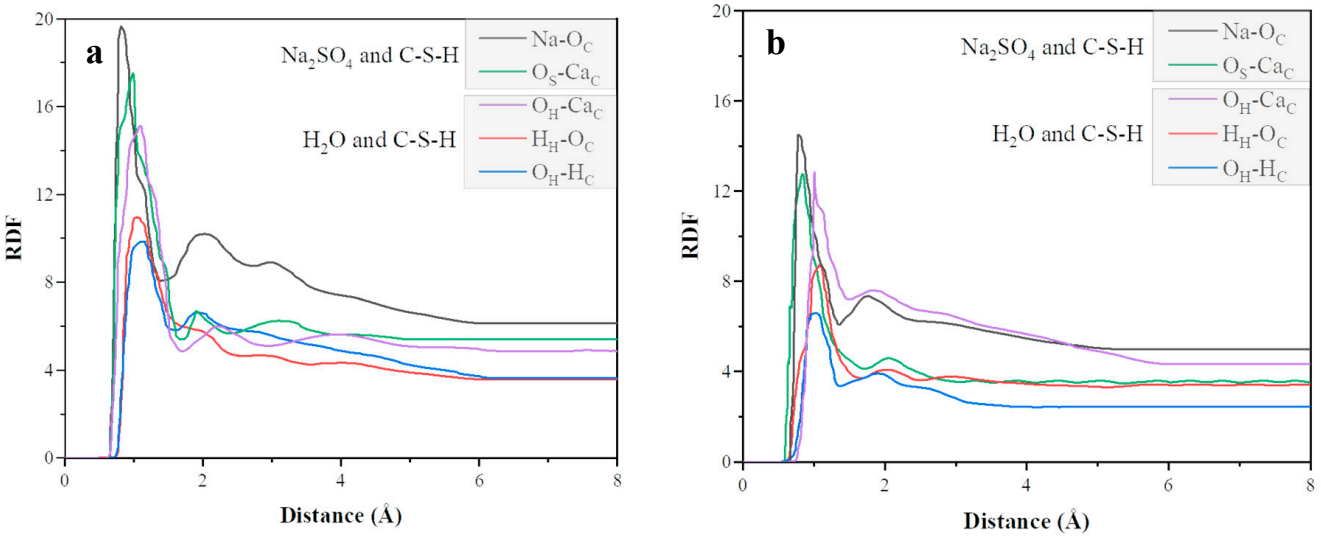


Figure 13. RDF results between sodium sulfate solution and C-S-H. (**a**) Without CN; (**b**) with CN.

Figure 13b presents the RDF results for the CN solution, where a decrease in the peak value for O_S-Ca_C is evident. This suggests that the presence of CN reduces the spatial correlation between Na_2SO_4 and C-S-H, lowers the coordination number between atomic pairs, and mitigates the corrosive effect of SO_4^{2-} on the matrix. Additionally, the decrease in the peaks corresponding to O_H-H_C, O_H-Ca_C, and H_O-O_C coordination indicates that the adsorption between C-S-H and water molecules is weakened, and CN alleviates the erosion of C-S-H by water.

Under the interaction of O_{CN}-H_C, O_{CN}-Ca_C, and H_{CN}-O_C atom pairs (Figure 11), the CN adsorbs onto the surface of C-S-H, forming a protective layer that mitigates the corrosion of C-S-H by SO_4^{2-} and water molecules. Additionally, the adsorption of the CN by SO_4^{2-} reduces the amount of SO_4^{2-} adsorbed by C-S-H, thereby inhibiting the formation of expansive products. The adsorption of water molecules by the CN further diminishes the number of water molecules involved in C-S-H adsorption, alleviating the erosion of C-S-H by water. In summary, the surface coating protection provided by the CN and its ability to absorb both SO_4^{2-} and water molecules are critical factors in significantly enhancing the sulfate corrosion resistance of the ECC.

The density distribution of water molecules along the CN adsorption direction (Z-axis) is shown in Figure 14a. The water molecule density reaches a maximum of approximately 1.4 g/cm^3 at 1.8 Å from the adsorption interface, indicating the strong hydrophilicity of C-S-H. The presence of the CN slightly decreases the maximum density of water molecules from 1.40 g/cm^3 to 1.39 g/cm^3, likely due to the hydrophilic CN adsorbing some water molecules and preventing them from approaching the C-S-H surface. Furthermore, the presence of the CN significantly reduces the density of water molecules at distances of 3–5 Å from the interface, as the CN occupies the positions previously held by water molecules after adsorbing onto the C-S-H surface.

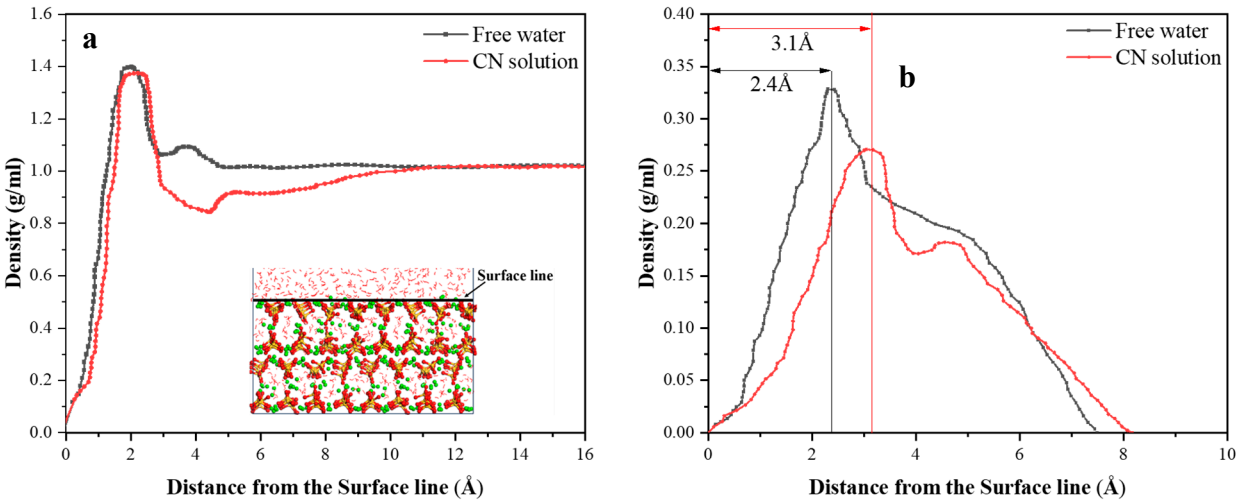


Figure 14. Density distribution results of water molecules and SO_4^{2-}. (**a**) Water molecules; (**b**) SO_4^{2-}.

The density distribution of SO_4^{2-} in Figure 14b exhibits a trend similar to that of water molecules. The presence of the CN reduces the maximum density of SO_4^{2-} and increases the distance between SO_4^{2-} and C-S-H from 2.4 Å to 3.1 Å. After the CN adsorbs onto the C-S-H surface, it occupies a spatial region between 2 and 4 Å from the surface, displacing SO_4^{2-} and thereby increasing the interatomic distance between SO_4^{2-} and C-S-H. This displacement weakens the interaction between the atomic pairs [51]. These findings further support the notion that the CN diminishes the interaction between water molecules, SO_4^{2-}, and C-S-H. The detailed adsorption patterns of sodium sulfate solutions, the CN, and C-S-H are illustrated in Figure 15.

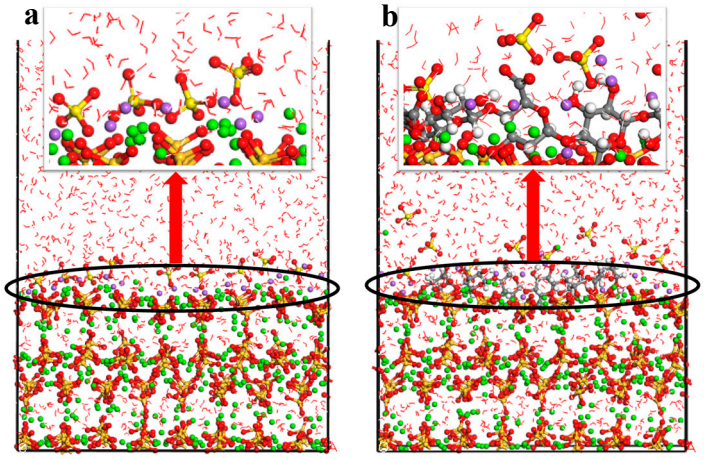


Figure 15. Adsorption snapshots of the models. (**a**) Without CN; (**b**) with CN.

During the simulation, both water molecules and SO_4^{2-} are in motion, and their movement can be quantified through the Mean Square Displacement (MSD) [52]. The diffusion (D) coefficient of the atoms is derived from the slope of the MSD curve. The MSD results for water molecules and SO_4^{2-} ions are presented in Figure 16a,b. It is evident that in the unincorporated CN model, both water molecules and SO_4^{2-} exhibit higher MSD values, indicating faster diffusion toward the interface. In this case, the water molecules and SO_4^{2-} are drawn to the active Ca and O atoms at the C-S-H interface, facilitating their rapid diffusion and subsequent corrosion reactions. In contrast, the presence of the CN binds some water molecules and SO_4^{2-} to its surface, thereby impeding their mobility, restricting their diffusion, and ultimately mitigating the interaction between water molecules, SO_4^{2-}, and the cement matrix.

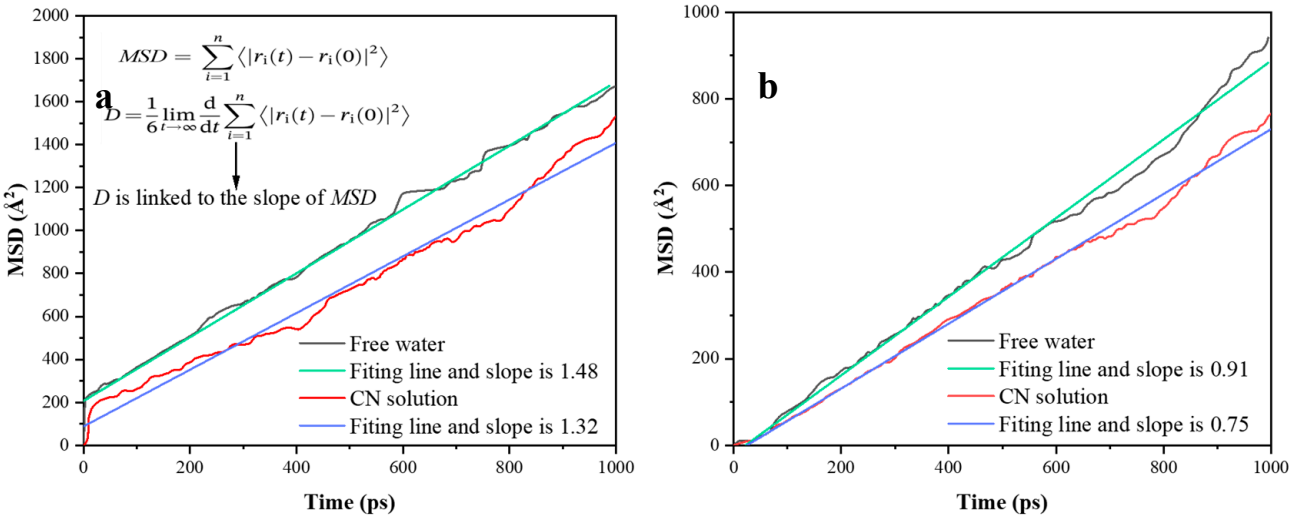


Figure 16. MSD results of water molecules and SO_4^{2-}. (**a**) Water molecules; (**b**) SO_4^{2-}.

5. Conclusions

(1) A 0.15% addition of cellulose nanocrystals (CNs) can increase the compressive strength and strain rate of ECCs by 12% and 54.77% and reduce the strain rate loss of ECC samples after 120 days of sulfate corrosion by 24.85%. However, excessive CN dosages may result in poor dispersion. The optimal CN dosage for achieving the desired improvements is 0.15%.

(2) Scanning electron microscopy (SEM) analysis reveals a reduction in silica fume content and an increase in the formation of ettringite and C-S-H within the CN-ECC sample group, leading to a higher matrix density compared to the control group (without the CN). The CN facilitates greater participation of silica fume in hydration reactions, thereby enhancing the hydration level of the binder system in CN-ECC.

(3) Molecular dynamics simulations demonstrate that the CN adsorbs onto the surface of C-S-H, forming a protective layer that prevents the infiltration of SO_4^{2-} and water molecules into the C-S-H structure. Additionally, the CN forms hydrogen bonds with SO_4^{2-} and water molecules, inhibiting the coordination between C-S-H and these molecules. This interaction restricts the diffusion rate of SO_4^{2-} and water molecules at the C-S-H interface, thereby mitigating the erosion of hydrated products caused by SO_4^{2-} and water molecules.

Author Contributions: Conceptualization, L.Y.; Methodology, L.Y. and B.X.; Software, X.X., D.M. and B.X.; Validation, S.N.; Formal analysis, X.M.; Investigation, L.Y., S.N., D.M. and B.X.; Writing—original draft, L.Y.; Supervision, B.X.; Project administration, B.X.; Funding acquisition, B.X. All authors have read and agreed to the published version of the manuscript.

Funding: This research was funded by the Project of Natural Science Foundation of Shandong Province (Grant number: ZR2021QE197) and Qingdao Agricultural University High level Talent Research Fund (Grant number: 1120711).

Institutional Review Board Statement: Not applicable.

Informed Consent Statement: Not applicable.

Data Availability Statement: The raw data supporting the conclusions of this article will be made available by the authors on request.

Acknowledgments: The authors acknowledge Shiyanjia Lab (www.shiyanjia.com, accessed on 25 June 2022) for providing the TEM test.

Conflicts of Interest: The authors declare no conflict of interest.

References

1. Li, V.C.; Wang, S.; Wu, C. Tensile strain-hardening behavior of polyvinyl alcohol engineered cementitious composite (PVA-ECC). *Mater. J.* **2001**, *98*, 483–492.
2. Li, V.C.; Bos, F.P.; Yu, K.Q.; McGee, W.; Ng, T.; Figueiredo, S. On the emergence of 3D printable engineered, strain hardening cementitious composites (ECC/SHCC). *Cem. Concr. Res.* **2020**, *132*, 106038. [CrossRef]
3. Zhu, H.; Zhang, D.; Li, V.C. Centrifugally sprayed engineered cementitious composites: Rheology, mechanics, and structural retrofit for concrete pipes. *Cem. Concr. Compos.* **2022**, *129*, 104473. [CrossRef]
4. Zhu, H.; Wang, T.Y.; Wang, Y.C.; Li, V.C. Trenchless rehabilitation for concrete pipelines of water infrastructure: A review from the structural perspective. *Cem. Concr. Compos.* **2021**, *123*, 104193. [CrossRef]
5. Yu, J.; Chen, Y.X.; Leung, C.K.Y. Micromechanical modeling of crack-bridging relations of hybrid-fiber strain-hardening cementitious composites considering interaction between different fibers. *Constr. Build. Mater.* **2018**, *182*, 629–636. [CrossRef]
6. Singh, S.B.; Munjal, P. Engineered cementitious composite and its applications. *Mater. Today Proc.* **2020**, *32*, 797–802. [CrossRef]
7. Li, V.C. On engineered cementitious composites (ECC): A review of the material and its applications. *J. Adv. Concr. Technol.* **2003**, *1*, 215–230. [CrossRef]
8. Zhu, J.X.; Weng, K.F.; Huang, B.T.; Xu, L.; Bai, J. Ultra-high-strength engineered cementitious composites (UHS-ECC) panel reinforced with FRP bar/grid: Development and flexural performance. *Eng. Struct.* **2024**, *302*, 117193. [CrossRef]
9. Bonfim, W.B.; de Paula, H.M. Characterization of different biomass ashes as supplementary cementitious material to produce coating mortar. *J. Clean. Prod.* **2021**, *291*, 125869. [CrossRef]
10. Zerihun, B.; Yehualaw, M.D.; Vo, D.H. Effect of agricultural crop wastes as partial replacement of cement in concrete production. *Adv. Civ. Eng.* **2022**, *2022*, 5648187. [CrossRef]
11. Zhang, Z.; Yang, F.; Liu, J.C.; Wang, S. Eco-friendly high strength, high ductility engineered cementitious composites (ECC) with substitution of fly ash by rice husk ash. *Cem. Concr. Res.* **2020**, *137*, 106200. [CrossRef]
12. Chen, H.; Yang, J. A new supplementary cementitious material: Walnut shell ash. *Constr. Build. Mater.* **2023**, *408*, 133852. [CrossRef]
13. Camargo-Pérez, N.R.; Abellán-García, J.; Fuentes, L. Use of rice husk ash as a supplementary cementitious material in concrete mix for road pavements. *J. Mater. Res. Technol.* **2023**, *25*, 6167–6182. [CrossRef]
14. Wu, M.; Zhang, Y.; Ji, Y.; She, W.; Yang, L.; Liu, G. A comparable study on the deterioration of limestone powder blended cement under sodium sulfate and magnesium sulfate attack at a low temperature. *Constr. Build. Mater.* **2020**, *243*, 118279. [CrossRef]
15. O'Connell, M.; McNally, C.; Richardson, M.G. Performance of concrete incorporating GGBS in aggressive wastewater environments. *Constr. Build. Mater.* **2012**, *27*, 368–374. [CrossRef]
16. Al-Dulaijan, S.U.; Maslehuddin, M.; Al-Zahrani, M.M.; Sharif, A.M.; Shameem, M.; Ibrahim, M. Sulfate resistance of plain and blended cements exposed to varying concentrations of sodium sulfate. *Cem. Concr. Compos.* **2003**, *25*, 429–437. [CrossRef]
17. Sahmaran, M.; Li, V.C.; Andrade, C. Corrosion resistance performance of steel-reinforced engineered cementitious composite beams. *ACI Mater. J.* **2008**, *105*, 243.
18. Abdulkadir, I.; Mohammed, B.S.; Liew, M.S.; Wahab, M.M.A. Modelling and optimization of the impact resistance of graphene oxide modified crumb rubber-ECC using response surface methodology. In *IOP Conference Series: Materials Science and Engineering*; IOP Publishing: Bristol, UK, 2021; Volume 1197, p. 012043.
19. Sabapathy, L.; Mohammed, B.S.; Al-Fakih, A.; Wahab, M.M.; Liew, M.S.; Amran, Y.H.M. Acid and sulphate attacks on a rubberized engineered cementitious composite containing graphene oxide. *Materials* **2020**, *13*, 3125. [CrossRef]
20. Liu, G.; Zhang, H.; Liu, J.; Xu, S.; Chen, Z. Experimental study on the salt freezing durability of multi-walled carbon nanotube ultra-high-performance concrete. *Materials* **2022**, *15*, 3188. [CrossRef]
21. Mohseni, E.; Miyandehi, B.M.; Yang, J.; YangYazdi, M.A. Single and combined effects of nano-SiO_2, nano-Al_2O_3 and nano-TiO_2 on the mechanical, rheological and durability properties of self-compacting mor tar containing fly ash. *Constr. Build. Mater.* **2015**, *84*, 331–340. [CrossRef]
22. Vanin, D.V.F.; Andrade, V.D.; Fiorentin, T.A.; Recouvreux, D.O.S.; Carminatti, C.A.; Al-Qureshi, H.A. Cement pastes modified by cellulose nanocrystals: A dynamic moduli evolution assessment by the impulse excitation technique. *Mater. Chem. Phys.* **2020**, *239*, 122038. [CrossRef]
23. Zhou, S.; Qiu, Z.; Strømme, M.; Wang, Z. Highly crystalline PEDOT nanofiber templated by highly crystalline nanocellulose. *Adv. Funct. Mater.* **2020**, *30*, 2005757. [CrossRef]
24. Lee, H.J.; Kim, S.K.; Kang, Y.; Kim, W. Fire resistance evaluation of fiber-reinforced cement composites using cellulose nanocrystals. *Adv. Concr. Constr.* **2019**, *8*, 311–320.
25. Lee, H.J.; Kim, W. Long-term durability evaluation of fiber-reinforced ECC using wood-based cellulose nanocrystals. *Constr. Build. Mater.* **2020**, *238*, 117754. [CrossRef]
26. Cao, Y.; Tian, N.; Bahr, D.; Zavattieri, P.D.; Youngblood, J.; Moon, R.J.; Weiss, J. The influence of cellulose nanocrystals on the microstructure of cement paste. *Cem. Concr. Compos.* **2016**, *74*, 164–173. [CrossRef]

27. Lu, M.; Zheng, Y.Y.; Yin, Z.Y. Investigating the consolidation of kaolinite with Molecular Dynamics: The micro effective stress principle. *Appl. Surf. Sci.* **2025**, *690*, 162653. [CrossRef]
28. Lu, M.; Zheng, Y.Y.; Yin, Z.Y. From sedimentation to consolidation of kaolinite: A molecular dynamic study. *Comput. Geotech.* **2024**, *170*, 106285. [CrossRef]
29. Lu, M.; Zheng, Y.Y.; Yin, Z.Y. A molecular dynamics study on the softening of kaolinite in water: Weakening of tensile property during stretching and disintegration of structure during soaking. *Comput. Geotech.* **2024**, *173*, 106562. [CrossRef]
30. Lu, M.; Diao, Q.F.; Zheng, Y.Y.; Yin, Z.Y.; Dai, Z. Influence of Water on Tensile Behavior of Illite through the Molecular Dynamics Method. *Int. J. Geomech.* **2024**, *24*, 04024024. [CrossRef]
31. Lu, Z.Y.; Yin, R.; Yao, J.; Zhao, B. Experimental and molecular dynamic study on the interfacial strengthening mechanism of PE fiber/cement mortar using advanced oxidation processes. *Constr. Build. Mater.* **2021**, *309*, 125144. [CrossRef]
32. Wang, P.; Qiao, G.; Guo, Y.; Zhang, Y.; Jin, Z.; Zhang, J. Molecular dynamics simulation of the interfacial bonding properties between graphene oxide and calcium silicate hydrate. *Constr. Build. Mater.* **2020**, *260*, 119927. [CrossRef]
33. Liu, Y.; Zheng, Y.; Lin, H.; Huang, G.; Fan, Q.; Meng, D. Calculation of contact angle via Young-Dupré equation with Molecular Dynamic Simulation: Kaolinite as an example. *Colloids Surf. A Physicochem. Eng. Asp.* **2024**, *697*, 134469. [CrossRef]
34. *GB/T50082-2009*; Standard for Test Methods of Long-Term Performance and Durability of Ordinary Concrete. Standerdization Administration of the People's Republic of China: Beijing, China, 2009.
35. Fan, Q.; Zheng, Y.; Meng, D.; Guo, Q.; Liu, Y.; Wu, H. Study on improving the performance of Engineered Cement-Based Composites by modifying binder system and polyethylene fiber/matrix interface. *Colloids Surf. A Physicochem. Eng. Asp.* **2025**, *707*, 135862. [CrossRef]
36. Fan, Q.; Zheng, Y.; Liu, Y.; Liu, Y.; Meng, X.; Guo, H.; Wang, Z. Effect of modified cellulose nanocrystals on the structure of calcium silicate hydrate studied by molecular dynamics simulation and experiment. *Langmuir* **2023**, *39*, 16244–16260. [CrossRef]
37. Cao, Y.; Zavaterri, P.; Youngblood, J.; Moon, R.; Weiss, J. The influence of cellulose nanocrystal additions on the performance of cement paste. *Cem. Concr. Compos.* **2015**, *56*, 73–83. [CrossRef]
38. Fan, Q.C.; Meng, X.; Li, Z.D.; Ma, G.Y.; Wang, Z.P.; Zhang, K.; Meng, D. Experiment and molecular dynamics simulation of functionalized cellulose nanocrystals as reinforcement in cement composites. *Constr. Build. Mater.* **2022**, *341*, 127879. [CrossRef]
39. Flores, J.; Kamali, M.; Ghahremaninezhad, A. An Investigation into the Properties and Microstructure of Cement Mixtures Modified with Cellulose Nanocrystal. *Materials* **2017**, *10*, 498. [CrossRef] [PubMed]
40. Fu, T.; Montes, F.; Suraneni, P.; Youngblood, J.; Weiss, J. The Influence of Cellulose Nanocrystals on the Hydration and Flexural Strength of Portland Cement Pastes. *Polymers* **2017**, *9*, 424. [CrossRef]
41. Zheng, D.; Yang, H.; Feng, W.; Fang, Y.; Cui, H. Modification mechanism of cellulose nanocrystals in cement. *Cem. Concr. Res.* **2023**, *165*, 107089. [CrossRef]
42. Chen, Y.; Zheng, Y.; Zhou, Y.; Zhang, W.; Li, W.; She, W.; Liu, J.; Miao, C. Multi-layered cement-hydrogel composite with high toughness, low thermal conductivity, and self-healing capability. *Nat. Commun.* **2023**, *14*, 3438. [CrossRef]
43. Wang, P.; Duan, Y.; Zheng, H.; Chen, Z.; Wang, M.; Wang, X.; Li, H.; Hou, D. Molecular structure and dynamics of water on the surface of cement hydration products: Wetting behavior at nanoscale. *Appl. Surf. Sci.* **2023**, *611*, 155713. [CrossRef]
44. Ramasamy, J.; Amanullah, M. Nanocellulose for oil and gas field drilling and cementing applications. *J. Pet. Sci. Eng.* **2020**, *184*, 106292. [CrossRef]
45. Liu, K.; Cheng, X.; Ma, Y.; Gao, X.; Zhang, C.; Li, Z.; Zhuang, J. Analysis of interfacial nanostructure and interaction mechanisms between cellulose fibres and calcium silicate hydrates using experimental and molecular dynamics simulation data. *Appl. Surf. Sci.* **2020**, *506*, 144914. [CrossRef]
46. Fan, Q.; Zheng, Y.; Yang, Y.; Liu, S.; Meng, D.; Guo, Q.; Liu, Y. Effect of interface properties between functionalized cellulose nanocrystals and tricalcium silicate on the early hydration mechanism of cement. *Colloids Surf. A Physicochem. Eng. Asp.* **2024**, *698*, 134552. [CrossRef]
47. Lu, Z.; Yu, J.; Yao, J.; Hou, D. Experimental and molecular modeling of polyethylene fiber/cement interface strengthened by graphene oxide. *Cem. Concr. Compos.* **2020**, *112*, 103676. [CrossRef]
48. Hou, D.; Lu, Z.; Li, X.; Ma, H.; Li, Z. Reactive molecular dynamics and experimental study of graphene-cement composites: Structure, dynamics and reinforcement mechanisms. *Carbon* **2017**, *115*, 188–208. [CrossRef]
49. Lv, C.; Xue, Q.; Xia, D.; Ma, M.; Xie, J. Effect of chemisorption structure on the interfacial bonding characteristics of graphene-polymer composites. *Appl. Surf. Sci.* **2012**, *258*, 2077–2082. [CrossRef]
50. Fan, Q.; Wang, Z.; Meng, X.; Zhang, K.; Ma, G.; Li, Z.; Meng, D. Multi-scale analysis of the strengthening mechanism of functionalized graphene as reinforcement in cement composites. *Colloids Surf. A Physicochem. Eng. Asp.* **2022**, *651*, 129729. [CrossRef]

51. Fan, Q.; Liu, Y.; Zheng, Y.; Meng, D.; Guo, Q.; Zheng, H.; Guo, B.; Liao, W. The microscopic reinforcement mechanism of Zhuhai soft soil by cement-based stabilizer: From microscopic characterization to molecular dynamics simulation. *Appl. Surf. Sci.* **2025**, *681*, 161574. [CrossRef]
52. Fan, Q.; Zheng, Y.; He, C.; Meng, D.; Guo, Q.; Liu, Y. Effect of interfacial properties between polyethylene and polyvinyl alcohol fiber/cement matrix on properties of mortar and ECC. *Struct. Concr.* **2024**, 1–16. [CrossRef]

Disclaimer/Publisher's Note: The statements, opinions and data contained in all publications are solely those of the individual author(s) and contributor(s) and not of MDPI and/or the editor(s). MDPI and/or the editor(s) disclaim responsibility for any injury to people or property resulting from any ideas, methods, instructions or products referred to in the content.